Downrange manoeuvre and oscillation suppression of a self-regulating centrifugally deployed flexible heat shield using a controlled reaction wheel

Rui Wu[a,c,*], Peter C.E. Roberts[a], Constantinos Soutis[b], Carl Diver[d]

[a] School of Mechanical, Aerospace and Civil Engineering, The University of Manchester, UK
[b] The University of Manchester Aerospace Research Institute, UK
[c] State Key Laboratory of Robotics and Systems (Harbin Institute of Technology), Harbin 150080, PR China
[d] School of Engineering, Manchester Metropolitan University, UK

ABSTRACT

A recent study has introduced a flexible deployable heat shield that passively deploys and stiffens due to centrifugal forces generated from a self-regulated autorotation. This paper demonstrates that the heat shield is similar to a PI controlled second order nonlinear system, which explains why the deployment is accompanied by a limit cycle structural oscillation that persists throughout a simulated re-entry. The heat shield design offers a unique capability to actively adjust the deployment using conventional attitude control devices. This operation is explored by simulating the re-entry of a CubeSat-sized vehicle equipped with an off-the-shelf reaction wheel controlled by a switching phase shift controller and gain-scheduled controllers. The effects of the control parameters are investigated, and successful oscillation suppression as well as an open-loop downrange manoeuvre of over 300 km is predicted for re-entry from low earth orbit.

1. Introduction

Deployable aerodynamic decelerators for atmospheric entry have been attracting increasing attention due to the demand for a next generation Mars entry system for heavy payloads, as well as a small recoverable orbital scientific platform, such as a CubeSat that can de-orbit and recover the payload using a re-entry vehicle [1–9]. The advantages of deployable heat shields over conventional rigid ones mainly come from two aspects [4,10]:

1. Low ballistic ratio (defined as m/SC_D) under the deployed condition leads to a higher deceleration in the upper atmosphere and thus reduced thermal load, as well as providing sufficient deceleration through planetary atmospheres that are less-dense than the Earth's (e.g. Mars), or even soft landing without a parachute system;
2. When stowed, the heat shield can be fitted into a limited space determined by the launch vehicle fairing or the acceptable payload volume.

Current developments mostly focus on two types of structures: the inflatable and the mechanically deployable structures. The inflatable structures are based on flexible thermal protection materials supported by air-tight chambers that deploy and stiffen when inflated by an on-board gas source or ram air [11–16]. The mechanically deployable structures are usually umbrella-like mechanisms consisted of rigid components as the skeleton and flexible thermal protection materials as the skirt [4,17–19].

Meanwhile, a new type of centrifugally deployed heat shield has been proposed in a previous study by the authors [20]. The core of the concept is a flexible conical shell made of ceramic fabric. Since local reinforcements are applied along an origami pattern, the shell naturally buckles along the pattern and forms a spiral shape when folded, as shown in Fig. 1. The spiral shape generates a roll-torque when descending through an atmosphere and leads to autorotation. In turn, the spin progressively flattens the shell, reducing the induced roll-torque. The rate of autorotation is thereby determined by the shell's deployment condition, and converges to a value where the centrifugal force on the flexible shell is in equilibrium with the aerodynamic load, thus enables a self-regulated spin and deployment. In this way, the structure is deployed and stiffened by inertia force generated from motion (i.e. centrifugal force from autorotation) rather than elastic forces from solid or gaseous materials, and as shown by the previous study, it could realise a CubeSat-sized re-entry vehicle that is lightweight, concise and high packing density [20].

Besides decelerating the payload while surviving aeorthermodynamic heating, advanced missions also require the entry vehicle to be

---

Nomenclatures

|	
a, b	downrange control parameters
a_{dec}	deceleration of vehicle
C_D	drag coefficient
f	natural frequency of the oscillatory motion
F	ratio of reaction wheel angular velocity and wheel maximum (saturated) speed
g	gravitational acceleration
i	control signal
I	angular inertia
l	base diameter of the fully deployed heat shield
m	total mass of vehicle
M	total deploying moment
M_a	anti-deploying moment from aerodynamic force
M_E	anti-deploying moment from elastic force
M_{FC}	deploying moment from centrifugal force
M_g	deploying moment from axial deceleration
$N_{torque\ factor}$	Torque factor
q	dynamic pressure
S	reference surface area of the vehicle
St	Strouhal Number
t	time
T_0	period of natural oscillation
v	descending velocity
θ	deployment angle
ω	spin rate of autorotation
ρ_S	shell surface density
T	Roll-torque
CG	Centre of Gravity
$IRVE$	Inflatable Re-entry Vehicle Experiment
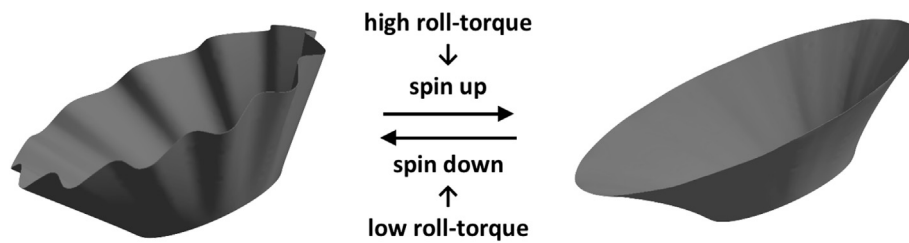
Fig. 1. Shape of the centrifugally deployed flexible heat shield generated from FE simulation, showing that equilibrium can be achieved between the partially folded condition (left) and the fully deployed condition (right) when the centrifugal force (due to autorotation) on the shield balances the aerodynamic force [20].

manoeuvrable in order to actively adjust the trajectory and enable a precise landing [21]. For a ballistic vehicle, this is usually achieved using a small lifting force generated by shifting the vehicle Centre of Gravity (CG) or changing the aerodynamic shape. The Inflatable Re-entry Vehicle Experiment (IRVE)-4 of NASA has proposed active CG shift to control the angle of attack of a 3-m diameter inflatable aeroshell [13]. Meanwhile, a number of studies on inflatable aeroshells with the stacked tori configuration similar to the IRVE have demonstrated different ways to either permanently or actively vary the shape of the aeroshell. Some studies have proposed to deform the whole aeroshell by canting the tori [21], sliding the tori perpendicular to the initial axis of symmetry [22,23], or morphing the tori using actuators [24]. Other concepts includes adding actuated flaps/trim tabs or compressible outer torus to change the aeroshell's centre of pressure [21,23]. On the other hand, mechanically deployable heat shields can also generate lift by having a permanent unsymmetrical shape when deployed [25]. Alternatively, an umbrella-like structure can realise variable frontal area

(thus ballistic ratio) by actively controlling the extend of deployment, thus enabling downrange control [17].

In comparison with inflatable and mechanically deployable heat shields, the centrifugally deployed heat shield offers a unique drag modulation capability by actively controlling the extent of deployment using conventional attitude control devices. This is because the centrifugal force, which deploys and stabilises the structure, depends on the vehicle's autorotating (rolling) motion. Therefore, when centrifugal force is altered by actively adjusting the roll rate using an actuator, the heat shield will deploy to a varied extent where it re-balances with the aerodynamic load, and effectively changes deployed drag area and therefore the trajectory.

Nevertheless, the reliance on centrifugal force and the structural flexibility also leads to problems. Lifting manoeuvres are not feasible since a non-zero angle of attack can not be maintained without conning motion as a result of gyroscopic effects on the rotating vehicle. A previous numerical study has also revealed an oscillatory deploying-
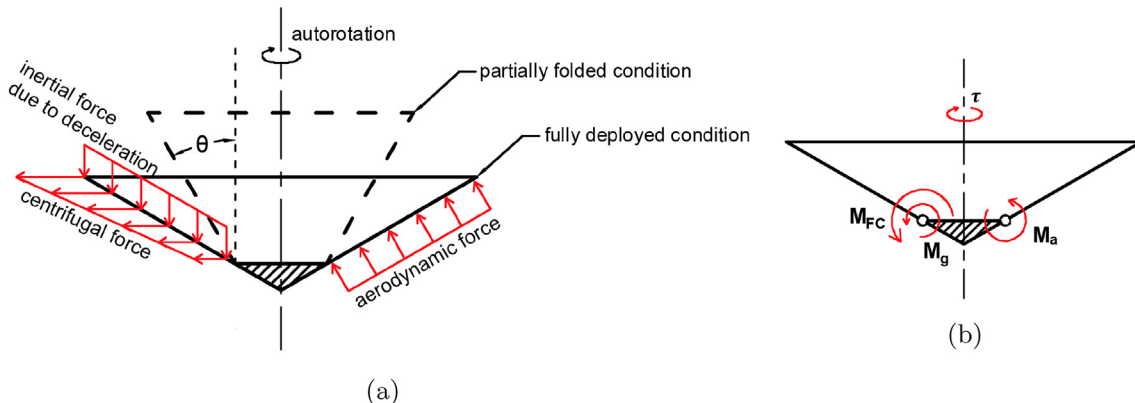
Fig. 2. Schematic view of the centrifugally deployed heat shield, (a) showing the three types of forces that contribute to the shield's deployment, and (b) the resulting torques with respect to the root of the shield, M_{FC}, M_g and M_a.

folding motion of the undamped heat shield throughout the descent [20].

The present work is a proof-of-concept study that focuses on utilising a reaction wheel to actively manipulate the extend of deployment and therefore, provides a way to suppress the oscillation. The feasibility to adjust the downrange trajectory using such a system is also discussed.

2. Analyses on the heat shield system

The proposed control method uses a single reaction wheel to adjust the rate of autorotation and thereby influence the deployment angle. Therefore, the analyses focus on the deploying-folding motion of the flexible heat shield as well as the autorotation of the vehicle, and all the analyses reported here are based on an aeroshell pointing stably into the flow with zero angle of attack, while the pitching and yawing motions as well as the gyroscopic effects from the autorotation are not considered. For a preliminary study, this is a reasonable simplification since the objective is to reveal the baseline effect of the proposed control, whilst the six Degree-of-Freedom (DoF) flight dynamics requires significantly more computational resource and is not analysed here.

During entry, the deployment of the heat shield is determined by three moments of forces (Fig. 2): the deploying moment due to centrifugal force M_{FC}, the deploying moment due to axial deceleration M_g, and the anti-deploying moment from aerodynamic load M_a. The moments are calculated as scalars with respect to the root of the shell and with directions shown in Fig. 2b. The total deploying moment M is:

$$M = M_{FC} + M_g - M_a \tag{1}$$

Then the shell deployment angle θ can be expressed as below, where I_{deploy} is shell's inertia associated with the deploying/folding motion. The shell is therefore a second order dynamic system.

$$\theta = \iint \frac{M}{I_{deploy}} \cdot dt \cdot dt \tag{2}$$

Based on the understanding of the heat shield's structural dynamics [20], a block diagram of the heat shield is constructed, as shown in Fig. 3. Ignoring the active control from the reaction wheel controller,

the heat shield can be treated as a second order system regulated by feedback from the three deploying/anti-deploying moments M_{FC}, M_g, and M_a [20]:

$$M_{FC} \propto \omega^2(\theta + 1.38)\cos\theta \tag{3}$$

$$M_g \propto a_{dec}\sin\theta \tag{4}$$

$$M_a \propto q(\theta - 0.407)\sin\theta \tag{5}$$

where ω is the rate of autorotation, q is dynamic pressure, and a_{dec}, the vehicle axial deceleration can be derived using Newton's law of motion:

$$a_{dec} = \frac{qSC_D}{m} \propto q(\theta - 0.347) \tag{6}$$

where S is shield reference area, C_D is drag coefficient, and m is vehicle mass. Substituting Equation (6) into (4), we have:

$$M_g \propto q(\theta - 0.347)\sin\theta \tag{7}$$

Using the equations above, Equation (2) can be simplified to:

$$\ddot{\theta} \approx \omega^2(0.700\theta + 0.963)\cos\theta - q(9.31\theta - 3.99)\sin\theta \tag{8}$$

Since the variation of v is usually minor except in the less-important low-speed regime, the dynamic pressure q can be regarded as constant. Meanwhile, since θ usually has values between $\pi/6$ and $\pi/3$ (30° ∼ 60°), the θ-M_g and θ-M_a relationships are near linear (Equations (4) and (5)), M_g and M_a can be treated as Proportional (P) control. M_{FC} contains an Integral (I) control component since ω is a result of integrated aerodynamic torque:

$$\dot{\omega} = \frac{\tau(\theta)}{I_{spin}(\theta)} \tag{9}$$

where τ is the roll-torque, and I_{spin} is the vehicle axial angular inertia. Both are calculated with respect to the vehicle axis, and are functions of θ. τ is treated as a scalar, and is set to positive/negative when it accelerates/decelerates the autorotation.

Therefore, the whole system is similar to a second order system regulated by a PI controller, while analytical analysis is difficult due to the complexity and non-linearity. According to Fig. 3, the behaviour of the system can be influenced by three parameters: the vehicle mass, the
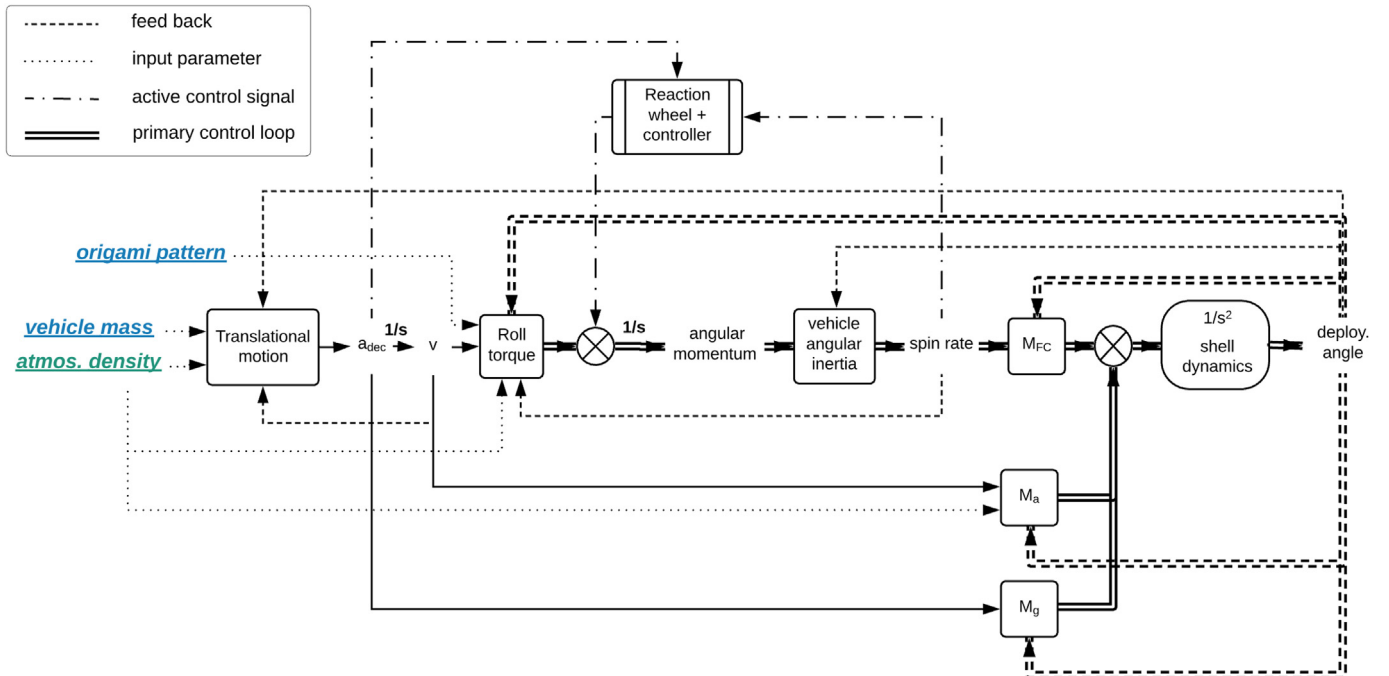

Fig. 3. Block diagram of the heat shield assuming zero angle of attack, with the primary feedback loops emphasised by double lines.

origami pattern, and the atmospheric density.

Simulations have shown that a limit cycle oscillation of the flexible heat shield exists within nearly the whole flight regime, which leads to variations in C_D and thus fluctuates the deceleration. This phenomenon can be seen in Fig. 10, where rapid fluctuations in deployment angle (for the uncontrolled scenarios with $a = b = 0$) are accompanied by fluctuations in deceleration. The vibration may cause damage to a payload especially when it has low natural frequencies (that is close to the oscillation frequency, which is usually 0.1 Hz ~ 10 Hz depending on the flight regime). Thus efforts are made to suppress this oscillation.

To enable oscillation suppression, spin rate and axial deceleration are measured and fed into the reaction wheel controller, which controls a reaction wheel that exerts an axial torque to stabilise the oscillation of spin rate and thus stabilise the deployment angle. Spin rate measurement is used to indicate the deployment angle, since the latter is difficult to measure, and the oscillation of the two are strongly coupled (due to the dependence of spin angular inertia on deployment angle, Equation (9)) with nearly no phase difference (since the dynamics of the shell deployment is significantly faster than the vehicle spinning dynamics, or in other words, the integral gain is low). The axial deceleration is used to compute a control parameter as discussed later.

Similarly, the reaction wheel is also used to adjust the overall deployment angle and enable open-loop downrange manoeuvre through drag modulation. This is achieved by varying the overall angular momentum of the system to increase/decrease M_{FC}, which leads to a biased deployment condition. Aerodynamic drag is thereby manipulated as it depends on the deployment angle. To be noted, the present work only demonstrates the feasibility to achieve extended/shortened downrange trajectory, while the control method to carry out a guided re-entry is not discussed.

Assume the maximum torque from the reaction wheel has a magnitude of τ_{wheel}, then the wheel outputs a torque of $i\tau_{wheel}$ when the throttle is set to i ($i \in [-1,1]$), and Equation (9) becomes:

$$\dot{\omega} = \frac{\tau_{aero.} + i\tau_{wheel}}{I_{spin}} \tag{10}$$

The detailed control strategy is shown in Fig. 4. Phase shift control is an existing method that has been used to suppress the thermal-acoustic oscillation of gas turbines. Its popularity comes from its simplicity, and thus the ability to survive in harsh environment, as well as the low requirement for knowledge of the complicated and highly non-linear system [26,27]. For the same reason it is proposed for oscillation suppression of the present heat shield, as it is a non-linear system that requires the control power and complexity to be minimised. The phase shift controller simply applies a time delay $K_T \cdot T_0$ to the input spin rate signal, and then outputs the difference between the original and the delayed signal (Fig. 4). The measurement of axial deceleration is used to determine the control parameter T_0 for the phase shift controller, which is explained in details in section 4. In the present proof-of-concept study, K_T is set to 0.25 after a series of trials since it provides effective oscillation suppression with a low requirement on actuator torque. Such a controller mimics a proportional-differential controller when the input is sinusoidal, but is less sensitive to noise. The input spin rate signal has a near sinusoidal component due to the oscillation, and a non-zero component that varies slowly during descent, which represents the autorotation. Therefore, the input spin rate signal can be assumed as $i_0 = \sin(2\pi t/T_0) + C(t)$, where $\sin(2\pi t/T_0)$ is the sinusoidal oscillation, and $C(t)$ is the non-zero component. With $K_T = 0.25$ the output will be:

$$i_1 = \sin\left(\frac{2\pi(t - 0.25T_0)}{T_0}\right) + C(t - 0.25T_0) - \sin\left(\frac{2\pi t}{T_0}\right) - C(t)$$
$$\approx -\cos\left(\frac{2\pi t}{T_0}\right) - \sin\left(\frac{2\pi t}{T_0}\right) = -\frac{T_0}{2\pi} \cdot \dot{i}_0 - i_0 \tag{11}$$

Note that the term $C(t - 0.25T_0) - C(t)$ is neglected. According to Equation (11), it can be seen that the output from the phase-shifter is a linear combination of a term containing the time derivative of the oscillation ($-\frac{T_0}{2\pi} \cdot \dot{i}_0$) and another term proportional to the oscillation ($-i_0$). It thereby functions as a PD controller to suppress this oscillation. i_1 is then normalised to unity before feeding into the anti-saturation controller.

In fact, the ratio between P ad D gains can be adjusted by tuning K_T. By re-writing Equation (11) as $i_1 \approx -2\sin(K_T\pi)\cos(2\pi t/T_0 - K_T\pi)$, it can be seen that $K_T \rightarrow 0$ gives a pure D controller, but is sensitive to noise since $i_1 \rightarrow 0$. K_T gives a pure P controller, which lacks the D component.

A major drawback of phase shift controllers is that they may induce the so called secondary peak, or in other words, the instability induced by the controller in frequencies away from the operation frequency [28,29]. In the present research, such instability is observed, but is a non-essential problem considering its low amplitude, as further discussed in section 4.

The downrange controller alters the deployment angle and drag coefficient through gain scheduling, which reduces the throttle when
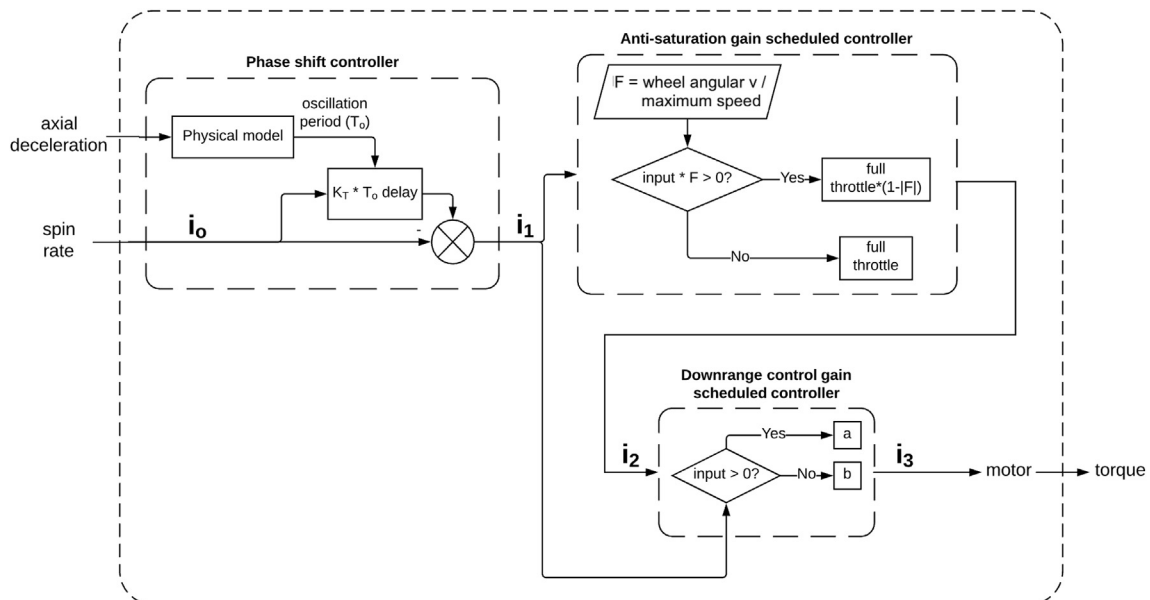

Fig. 4. Control algorithm of the reaction wheel controller.

the throttle is negative/positive and thus favours the increment/reduction of vehicle spin rate (Fig. 4):

$$i_3 = a\, i_2 \quad \text{if} \quad i_2 > 0 \tag{12}$$

$$i_3 = b\, i_2 \quad \text{if} \quad i_2 \leq 0 \tag{13}$$

Downrange is shortened when $a > b$, which favours the increment of spin rate and thereby facilitates deployment and leads to a higher aerodynamic drag.

Momentum saturation is inevitable when a biased control is applied, which requires an anti-saturation control. As can be seen in Fig. 4, the function of the de-saturation gain scheduling is to reduce the throttle when the motor is accelerating (when $i_1 F > 0$) and thereby tends to reduce the motor speed:

$$i_2 = i_1(1 - |F|) \quad \text{if} \quad i_1 F > 0 \tag{14}$$

$$i_2 = i_1 \quad \text{if} \quad i_1 F \leq 0 \tag{15}$$

where i_1 is the output from the phase shift controller, and F is the ratio of the wheel angular velocity and wheel maximum (saturated) speed, as shown in Fig. 4. In this way, the controller tends to bring the wheel speed to zero and thereby prevents momentum saturation.

The simulated effects of the controller are discussed with more details in section 4 and 5.

3. Parameter study on the oscillatory behaviour

The results discussed in the present research are generated from a numerical simulator developed in Simulink. The simulator is based on Newtonian aerodynamic equations while assuming zero angle of attack, and Newton's second law is used to describe the point mass dynamics of the vehicle. The previous structural dynamic model is also incorporated to include the deploying/folding behaviours of the flexible shield [20]. It should be noted that the Newtonian method only provides a rough estimation of the base line behaviour for subsonic flight conditions. All the results are generated with a maximum time step of 0.5 ms using a variable-step continuous explicit solver (ode45).

It also worth noticing that the simulator has not included structural damping since damping depends on various unknown factors such as specific material selection and layup. This could lead to an overestimation of oscillation amplitude. However, the structural damping in the design is expected to be weak considering the low heat shield thickness (~1 mm).

A typical limit cycle oscillation observed in the simulations is shown in Fig. 5, which is the result on a CubeSat-sized vehicle with the baseline design [20], 3 kg entry mass, and under a flight condition at 30 km altitude during re-entry from LEO. The initial condition (marked out in Fig. 5) assumes a near-fully deployed state with $\theta = 0°$ and $\dot{\theta} = 0°$, and $\dot{\theta}$ is set to zero every time when the extreme deployment angle ($\theta = 0°$ or $\theta = 60°$) is reached, representing an inelastic constraint. Referring to Fig. 3, running cases which neglect M_g and the coupling between deployment angle and spin angular inertia (by setting I_{spin} to constant, according to Equation (9)) shows that the oscillation is unrelated to these factors. In fact, the oscillatory behaviour is due to the integration component that determines M_{FC} (equation (9)). The aerodynamic roll torque is numerically evaluated using Newtonian method, which assumes the shield to have an ideal origami shape. The result is shown in Fig. 6, with its maximum value normalised to unity. The torque depends on deployment angle and the slope of flow velocity vector with reference to the rim of the heat shield. It worth noticing that this slope is proportional to the dimensionless Strouhal Number:

$$St = \frac{\omega \cdot l}{v} \tag{16}$$

It can be seen from Fig. 6 that the aerodynamic roll-torque is generally inversely-related to deployment angle. Therefore, when deployment angle is instantaneously increased from an equilibrium condition

(where $\tau = 0$ thus $\dot{\omega} = 0$ under static condition) due to oscillation, the roll-torque τ becomes negative. This negative torque then integrates over half oscillation period to reduce spin rate (equation (9)) and thus deployment angle with a phase lag, which assists the oscillation. Meanwhile, the variation of velocity vector slope is minor during the oscillation and thus has minor effect. Therefore, the primary feedback loop in Fig. 3 that contains M_{FC}, or in other words, the integral component is the cause of the oscillation.

The three factors that determine the actual behaviour of the heat shield, as illustrated in Fig. 3, are listed below. Their effects on the oscillation are studied using simulations.

(1) Atmospheric density; simulation assumes Earth atmosphere with density values ranging from 150 km altitude to sea level;
(2) Characteristics of the origami pattern; in the simulation, the magnitude of aerodynamic roll torque varies from 0.25 to 2 times of the baseline design;
(3) Total mass of the vehicle; varies from 0.75 kg to 3 kg.

At each data point, the simulation assumes constant atmospheric density and runs until the magnitude and amplitude of deployment angle are stabilised. The simulator also assumes the vehicle axis to be along gravity unlike the real trajectory conditions which have shallow flight path angles at high altitudes. This simplification is made since the objective of this study is to reveal the basic dynamic behaviour of the heat shield, rather than the exact behaviour at various trajectory conditions.

The effect of factors (1), (2) and (3) are shown in Fig. 7, where torque factor is a value that is multiplied to the baseline aerodynamic roll torque to manipulate its magnitude: $\tau_{simulated} = N_{torque\ factor} \cdot \tau$. It can be seen that the limit cycle oscillation exists throughout the flight regime, while the amplitude usually increases during descent. Generally, increasing torque factor leads to higher oscillation amplitude. This is because a higher torque factor is equivalent to a higher gain in the integral component that causes the oscillation (equation (9)).

The figure also show that the oscillation amplitude is usually higher in denser atmosphere. This is simply due to the fact that the simulator assumes the speed of the deploying motion becomes zero every time it reaches maximum/minimum deployment angle (60°/30°), thus the oscillation amplitude is mechanically constrained. Therefore, the amplitude can be higher when the equilibrium deployment angle is further away from 30° and 60°, which is the case in dense atmosphere. Similarly, in dense atmosphere there is a trend of increasing oscillation
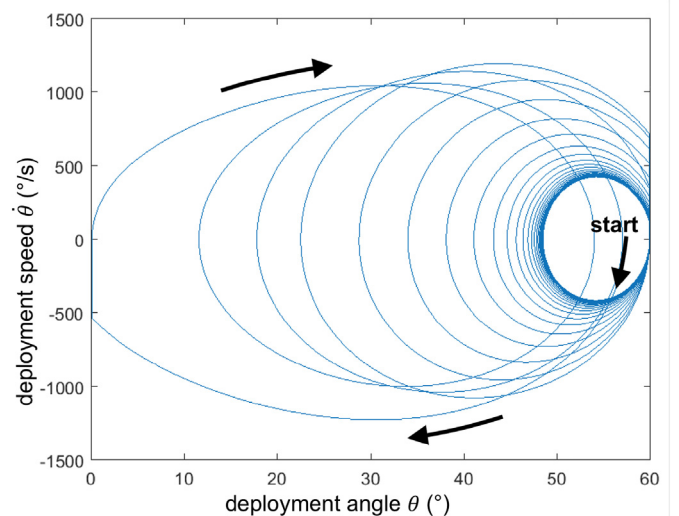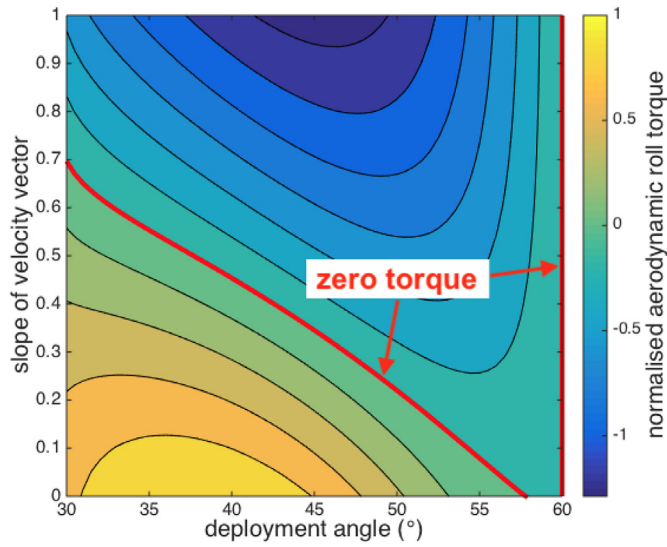

Fig. 5. A typical limit cycle oscillation from the simulations, where the deployment speed is the derivative of the deployment angle.
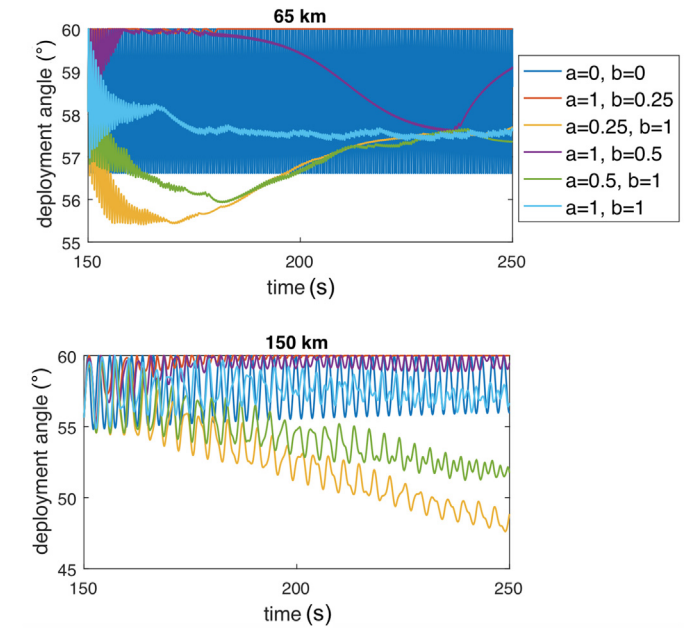
Fig. 6. Evaluation of the axial aerodynamic roll torque (with normalised magnitude) using deployment angle and the slope of velocity vector (i.e. the Strouhal number).

Fig. 8. Effect of the reaction wheel controller with various downrange control gains (*a* and *b*) at different altitudes, the controller is enabled at the simulation time of 150 s when equilibrium is reached, it can be seen that oscillation suppression is effective at lower altitude (in comparison with the dark blue line, which is the uncontrolled scenario with $a = 0$, $b = 0$ according to Equation (12) and (13)), while downrange control (with $a \neq b$) has effectively varied the average deployment angle before momentum saturation. (For interpretation of the references to colour in this figure legend, the reader is referred to the Web version of this article.)

amplitude with decreasing vehicle mass, which is particularly notable in Fig. 7b. This is because a lower mass leads to a higher equilibrium deployment angle that is further away from 30° and thus leads to higher oscillation amplitude.

Fig. 7 has also shown another trend of reducing oscillation amplitude due to decreasing vehicle mass, which exists at all the altitudes. This is because a lower mass leads to lower dynamic pressure, which, similar to a reducing torque factor, is equivalent to reducing the integration gain that causes the oscillation.

4. Oscillation suppression

The basic mechanism of the reaction wheel controller is already discussed in section 2: the controller feeds back and regulates the spin rate to alter the deployment angle. The control parameter T_0 in the phase shift controller is the period of the heat shield's natural oscillation, which can be approximated by Equation (17), as stated in Ref. [20]:
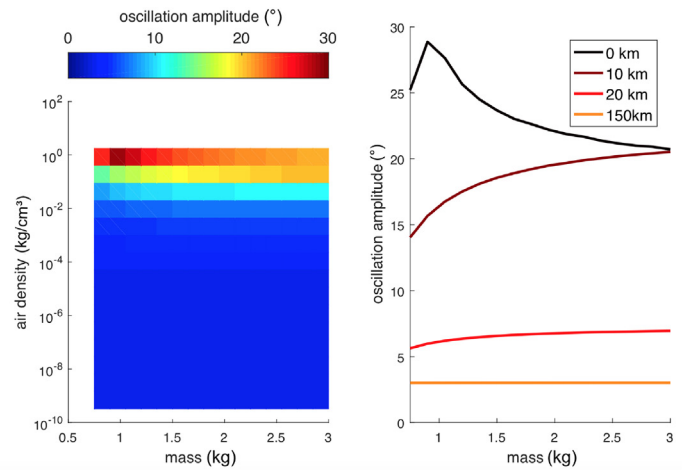
$$f = \frac{1}{2\pi}\sqrt{\frac{\frac{\partial M}{\partial \theta}}{I_{deploy}}}$$

(17)

where f is the natural frequency, M is the total deploying moment on the flexible shell evaluated according to equation (1), θ is deployment angle, and I_{deploy} is the deploying angular inertia of the shell. After simplification and assuming a deployment angle close to 60°, equation (17) becomes [20]:
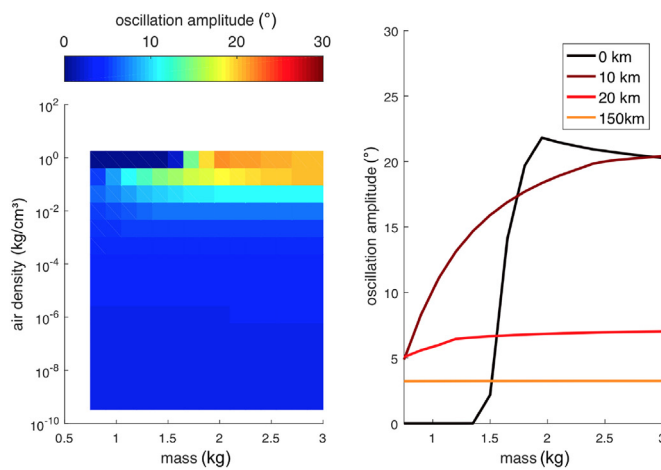
(a) Torque factor = 0.5

(b) Torque factor = 2

Fig. 7. Effect of vehicle mass, atmospheric density (or equivalent altitude on Earth) and magnitude of aerodynamic torque on the oscillation amplitude of deployment angle; it can be seen that the oscillation is common throughout different flight conditions, while the effects that reduces aerodynamic roll-torque always lead to a lower oscillation except at very low altitude (<10 km).

$$f \approx 0.49 \sqrt{\frac{a_{dec} \, (1.53 \, m - 1.21 \, l^2 \rho_S)}{l^3 \rho_S}} \quad \text{(Hz)} \tag{18}$$

where a_{dec} is deceleration (including the component of gravity along the vehicle's axis, in m/s^2), l is the heat shield base diameter when deployed, m is the vehicle's mass (kg), and ρ_S is the surface density of the shell (kg/m^2). The vehicle analysed in this section has a total mass of 3 kg, a surface density of 1.1 kg/m^2 and a base diameter of 0.7 m. Thus, equation (17) becomes:

$$f \approx 1.60 \sqrt{a_{dec}} \quad \text{(Hz)} \tag{19}$$

equation (19) provides simple predictions with the error <25% in comparison with simulation, and is incorporated into the reaction wheel controller.

Meanwhile, it should be noted that equation (1) ignores the elasticity and damping of the flexible shell, which is difficult to predict as it depends on the actual material and structural properties, whilst the elastic forces also depend on the initial deployment angle at the unloaded condition. However, the effect of elastic and damping force is expected to be weak as the aim of this heat shield design is to eliminate the dependence on elasticity while taking advantage of the structure supported by inertia force. Nevertheless, the anti-deployment moment of elastic force, M_E, is included in the numerical simulators since it has notable effect on the heat shield's deployment angle at high altitude where the aerodynamic effect is weak. Thus equation (1) becomes:

$$M = M_{FC} + M_g - M_a - M_E \tag{20}$$

Where M_E is evaluated based on the bending rigidity of the shield's root using linear beam theory by assuming a shell thickness of 1 mm, a Young's modulus of 5 MPa, and assumes bending occurs in a region within 10 mm from the shell's root. This provides a reasonable example to show the effect of elasticity, but is not based on any real designs. The deployment angle of the heat shield at unloaded condition is set to the minimum deployment angle (30 °), thus the elasticity provides an anti-deployment effect. The effect of M_E is illustrated by the trajectory simulation in Fig. 10, where the result on an uncontrolled vehicle without accounting for M_E is set in comparison with the same vehicle with M_E. It can be seen that the elastic force has notably reduced the deployment angle at high altitude and therefore increased the downrange, while its effect on the oscillatory behaviour is insignificant. Meanwhile, the spin rate at high altitude is increased by adding M_E since the heat shield requires higher centrifugal force to maintain its equilibrium deployment angle.

The sensors in the reaction wheel controller are set to have a sample rate of 1000 Hz, which provides a near ideal scenario. The controller output at 1000 Hz is then transferred to 50 Hz by averaging in every 20 ms, thus the motor is controlled at a rate of 50 Hz, and with its torque response assumed to be instantaneous for simplicity. As spin rate varies due to oscillation, the evaluated parameter T_0 is smoothed by a simple moving average filter with the length of 1000 to prevent the interference caused by this oscillation. This filter has shown no adverse effect since T_0 changes slowly through descent and is not sensitive to phase lag. With this filter, the noise in deceleration is generally irrelevant to the controller's performance and is not considered as an issue.

However, the spin rate measurement could have an excessive noise spectral density in the magnitude of $0.01°/s/\sqrt{\text{Hz}}$ (according to the gyro of a commercial IMU). This could be resolved using redundant sensors and signal processing techniques, but is not considered as the subject of this paper. Therefore, no noise is included in the simulations.

Since the simulation uses a baseline CubeSat-sized vehicle design, a reaction wheel is chosen accordingly to fit within such a system: the Sinclair Interplanetary RW3-0.060, which outputs torque of approx. ± 20 mNm with the wheel momentum within ± 0.18 Nms. Peak performance is achieved at roughly 25 W and 28 V. The reaction wheel assembly has a total mass of 226 g and a size of 77 mm × 65 mm × 38 mm [30].

To investigate the basic behaviours of the controlled vehicle, the simulator used to construct Fig. 7 is revised to include M_E, the reaction wheel controller, and the flight path angles that are determined using full trajectory simulation (Fig. 10). In order to eliminate the effect of initial conditions, the reaction wheel controller is turned on from the simulation time of 150 s when the spin rate is generally stabilised. The results at different altitudes are shown in Fig. 8. It can be seen that at lower altitude the oscillations are rapidly suppressed after the controller is enabled, whereas at higher altitudes where the oscillation suppression is slower since the phase shift controller becomes ineffective due to the large error in control parameter T_0. This is because equation (19) no longer holds when the dynamic pressure is low and elasticity has considerable effect on the shell's natural frequency.

Meanwhile, a small residual oscillation always emerge after the suppression of the original oscillation, which is caused by the coupling between the phase shift controller and the heat shield system, and has a frequency higher than the structural natural oscillation. The details of a typical residual oscillation is shown in Fig. 9. This phenomena is reminiscent of the so called secondary peaks caused by phase shift controllers used to suppress thermal acoustic oscillations of gas turbines [28]. However, this is not a critical issue considering the low oscillation amplitude, especially during the flight regime with higher dynamic pressure.

Then, the effect of oscillation suppression on the re-entry trajectory is assessed using the trajectory simulator, which assumes a re-entry starting from 15 km altitude at a velocity of 7800 m/s, with zero flight path angle, zero spin rate, and an initial deployment angle of 30 °. Simulations are terminated when the vehicle reaches 30 km altitude since the vehicle has already entered the uncritical low speed regime at this altitude.

According to the results shown in Fig. 10, the controller leads to effective oscillation reduction in both deployment angle and deceleration throughout descent. From the history of reaction wheel momentum it can be seen that the reaction wheel not only counteracts the oscillations that has relatively high frequency (0.1 Hz ~ 10 Hz), but also undesirably counteracts the overall variation of spin rate during the descent. As a result, momentum saturation is inevitable regardless of downrange control gains. Therefore, the de-saturation gain scheduling (Equations (14) and (15)) is always beneficial to the performance as it conserves some momentum that is useful for oscillation suppression when the reaction wheel approaches maximum speed, rather than inducing a hard-stop when the reaction wheel is saturated. With this
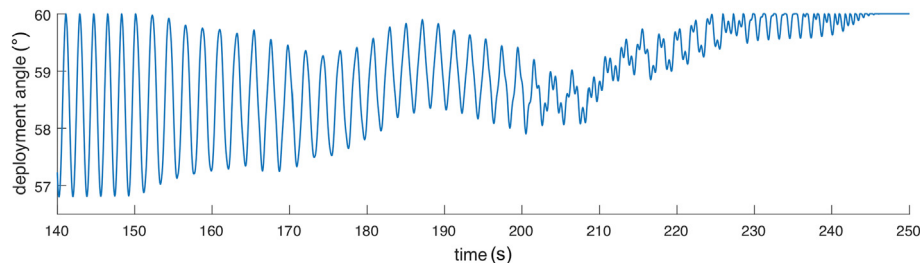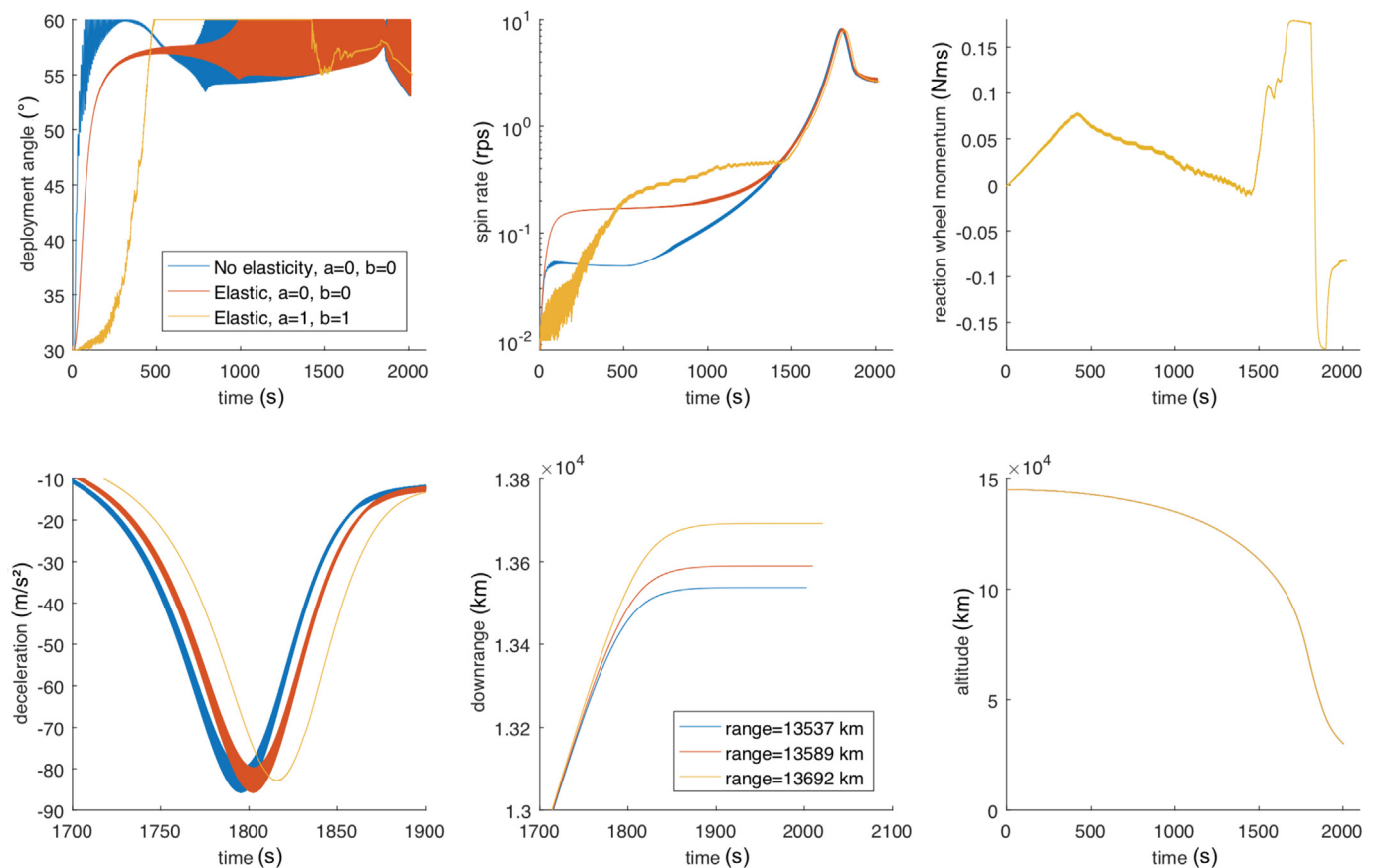

Fig. 9. Details of a typical residual oscillation, showing secondary peaks at a frequency higher than the natural oscillation.

Fig. 10. Trajectory simulation results without accounting for the shell's elasticity (blue), with elasticity (red), and with the controlled reaction wheel as well as elasticity (yellow), on a CubeSat-sized vehicle re-entering from 145 km LEO to 30 km altitude; it can be seen that for the uncontrolled scenarios ($a = b = 0$ according to Equation (12) and (13)) oscillation persists throughout the descent, which leads to fluctuation in deceleration. (For interpretation of the references to colour in this figure legend, the reader is referred to the Web version of this article.)

control strategy, a near saturated wheel could "harvest" momentum (from aerodynamic roll-torque) during oscillation and tend to bring the wheel speed back to zero. This is proven effective by the simulation as oscillation is suppressed even under the near-saturated condition before the peak dynamic pressure. Meanwhile, this de-saturation control also helps reducing reaction wheel power consumption as it reduces the motor speed.

5. Downrange control

As described in section 2, downrange manoeuvre can be achieved by manipulating the control gains a and b (Equation (12) and (13)), which leads to an overall spin-up or spin-down of the vehicle, thus influences the deployment angle, thereby determines the drag coefficient of the heat shield. According to Fig. 4, downrange can be shortened by letting $a > b$ as it tends to spin-up the vehicle, and vise versa. The effect of control parameters a and b is already validated by Fig. 8, which shows that a higher a/b ratio leads to a lower deployment angle until the re-action wheel is near-saturated. Meanwhile, due to the limited torque and momentum that the reaction wheel can output, the effect of downrange control is only eminent when the axial aerodynamic torque is low (at high altitude). Therefore, as supported by Fig. 8, the controller has a greater influence on the deployment angle at 150 km than at 65 km.

The effect of downrange control on re-entry trajectory is shown in Fig. 11 and summarised in Table 1. The setup is similar to the simulations reported in Fig. 10, with the elasticity factor M_E included. It has shown a total downrange variation of 322 km. According to the deceleration history, oscillation suppression is also achieved, while the

peak deceleration ($\sim 8\,g$) is independent of the trajectory. It should be noted that the downrange increment (202 km, with respect to the unbiased condition of $a = b = 1$) is higher than the decrement (120 km). The reason is discussed below.

It worth noticing that, according to the reaction wheel momentum history from Fig. 11, the controller counteracts the increasing spin rate at the start of re-entry for >200 s regardless of the downrange control gains (due to the phase shift controller). This affects the capability to reduce downrange, which requires high spin rate. It can also be seen from the figure that during the downrange-reducing manoeuvres (with $a = 1$, $b = 0.5$ and 0.25), the reaction wheel momentum is far from saturation throughout the high altitude flight regime. Therefore, the reaction wheel's capability is currently not fully utilised, and more effective manoeuvre can potentially be achieved by more sophisticated control algorithms.

6. Conclusions

In the previous study, a flexible heat shield that deploys and stiffens by a self-sustaining autorotation was designed. According to the present study, the passive self-regulated centrifugal deployment leads to a limit cycle structural oscillation, which persists throughout the simulated re-entry when assuming zero structural damping. This could be a problem for sensitive payloads. The present study also showed that the heat shield is similar to a second order nonlinear system controlled by a PI controller, where the integral component is causing the oscillation.

Meanwhile, since centrifugal force is determined by the vehicle's roll rate, the heat shield shape can be easily regulated using conventional attitude control devices. Therefore, an off-the-shelf reaction
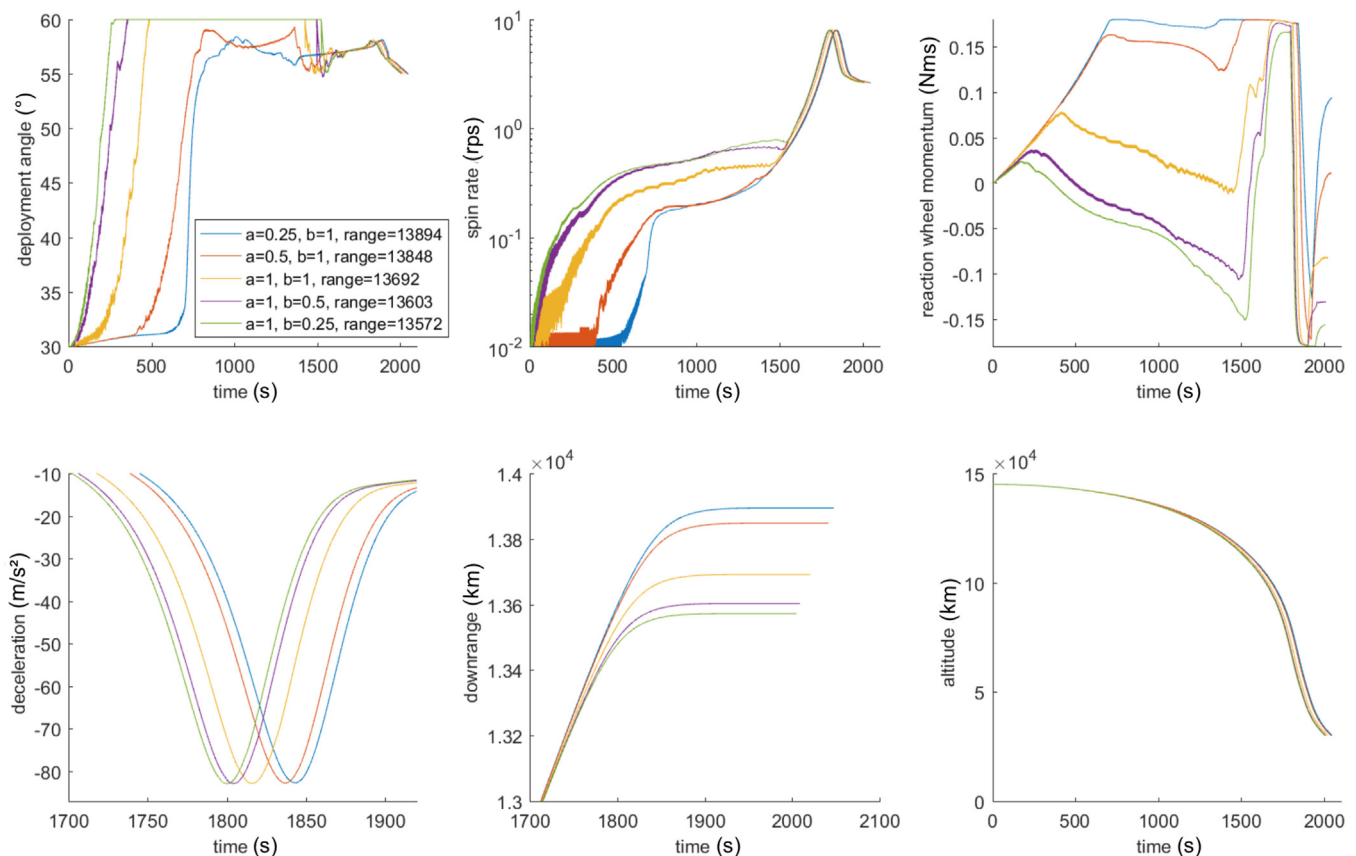
Fig. 11. Trajectory simulation results on the vehicle with different downrange control gains, downrange are reported in km, showing a downrange shift of >300 km and oscillation suppressed.

Table 1
Summary of the results from trajectory simulations of re-entry from 145 km altitude.

Control parameter	Downrange shift
a = 0.25, b = 1	202 km
a = 0.5, b = 1	147 km
a = 1, b = 1	0 km
a = 1, b = 0.5	−89 km
a = 1, b = 0.25	−120 km

wheel with a maximum power of 25 W and a mass of 226 g is proposed to regulate the autorotation (roll rate) of a CubeSat-sized vehicle and thereby achieve actively controlled deployment. The reaction wheel is controlled using a switching phase shift controller combined with gain scheduled controllers.

Specifically, the phase shift control realises oscillation suppression. The overall downrange manoeuvrability of over 300 km is achieved using a gain scheduled controller. Another gain scheduled controller keeps de-saturating the reaction wheel throughout the simulated re-entry. All the controls are successfully demonstrated by the numerical simulations based on Newtonian aerodynamics.

References

[1] M. Braun, P. Bruce, E. Levis, Strategies to utilize advanced heat shield technology for high-payload mars atmospheric entry missions, Acta Astronaut. 136 (2017) 22–33.

[2] J. Cruz, J. Lingard, Aerodynamic decelerators for planetary exploration: past, present, and future, AIAA Guidance, Navigation, and Control Conference and Exhibit, AIAA, 2006paper 2006-6792.

[3] R.D. Braun, R.M. Manning, Mars exploration entry, descent, and landing challenges, J. Spacecraft Rockets 44 (2) (2007) 310–323.

[4] G. Zuppardi, R. Savino, G. Mongelluzzo, Aero-thermo-dynamic analysis of a low ballistic coefficient deployable capsule in earth re-entry, Acta Astronaut. 127 (2016) 593–602.

[5] J. Andrews, K. Watry, K. Brown, Nanosat deorbit and recovery system to enable new missions, SSC11-X-3, Presented at the 25th AIAA/USU Conference on Small Satellites, Logan, Utah, USA, 8-12 August, 2011.

[6] D.M. Bose, J. Shidner, R. Winski, C. Zumwalt, F. Cheatwood, S.J. Hughes, The hypersonic inflatable aerodynamic decelerator (HIAD) mission applications study, AIAA Aerodynamic Decelerator Systems (ADS) Conference, AIAA, 2013paper 2013-1389.

[7] J. Virgili, P.C. Roberts, N.C. Hara, Atmospheric interface reentry point targeting using aerodynamic drag control, J. Guid. Contr. Dynam. 38 (3) (2015) 403–413.

[8] K. Yamada, Y. Nagata, T. Abe, K. Suzuki, O. Imamura, D. Akita, Suborbital reentry demonstration of inflatable flare-type thin-membrane aeroshell using a sounding rocket, J. Spacecraft Rockets 52 (1) (2014) 275–284.

[9] E. Fantino, M. Grassi, P. Pasolini, F. Causa, C. Molfese, R. Aurigemma, N. Cimminiello, D. de la Torre, P. Dell'Aversana, F. Esposito, et al., The small mars system, Acta Astronaut. 137 (2017) 168–181.

[10] I.G. Clark, A.L. Hutchings, C.L. Tanner, R.D. Braun, Supersonic inflatable aerodynamic decelerators for use on future robotic missions to mars, Aerospace Conference, 2008 IEEE, IEEE, 2008, pp. 1–17.

[11] B.P. Smith, C.L. Tanner, M. Mahzari, I.G. Clark, R.D. Braun, F.M. Cheatwood, A historical review of inflatable aerodynamic decelerator technology development, Aerospace Conference, 2010 IEEE, IEEE, 2010, pp. 1–18.

[12] H. Bohon, M. Mikulas, Development status of attached inflatable decelerators, J. Spacecraft Rockets 6 (6) (1969) 654–660.

[13] D. Litton, D. Bose, F. Cheatwood, S. Hughes, H. Wright, M. Lindell, S. Derry, A. Olds, Inflatable re-entry vehicle experiment IRVE-4 overview, 21st AIAA Aerodynamic Decelerator Systems Technology Conference and Seminar, AIAA, 2011paper 2011-2580.

[14] A. Mastropietro, J. Kempenaar, M. Redmond, M. Pauken, W. Ancarrow, First test flight thermal performance of the low density supersonic decelerator (LDSD) supersonic flight dynamics test (SFDT) vehicle, 45th International Conference on Environmental Systems, 2015.

[15] C. Tanner, J. Cruz, R. Braun, Structural verification and modeling of a tension cone inflatable aerodynamic decelerator, 51st AIAA/ASME/ASCE/AHS/ASC Structures, Structural Dynamics, and Materials Conference 18th AIAA/ASME/AHS Adaptive Structures Conference 12th, AIAA, 2010paper 2010-2830.

[16] D. Wilde, S. Walther, K. Pitchadze, S. Alexsaschkin, D. Vennemann, L. Marraffa, Flight test and ISS application of the inflatable reentry and descent technology

(IRDT), Acta Astronaut. 51 (1–9) (2002) 83–88.

[17] V. Carandente, R. Savino, New concepts of deployable de-orbit and re-entry systems for cubesat miniaturized satellites, Recent Pat. Eng. 8 (1) (2014) 2–12.

[18] D.L. Akin, The parashield entry vehicle concept-basic theory and flight test development, 4th AIAA/USU Small Satellite Conference, Logan, UT, Aug. 27-30, 1990, Proceedings. (A91-27376 10-18). Logan, 1 1990.

[19] E. Venkatapathy, K. Hamm, I. Fernandez, J. Arnold, D. Kinney, B. Laub, A. Makino, M. McGuire, K. Peterson, D. Prabhu, et al., Adaptive deployable entry and placement technology (ADEPT): a feasibility study for human missions to mars, 21st AIAA Aerodynamic Decelerator Systems Technology Conference and Seminar, AIAA, 2011paper 2011-2608.

[20] R. Wu, P.C. Roberts, C. Soutis, C. Diver, Flexible heat shields deployed by centrifugal force, Acta Astronaut. (2018), https://doi.org/10.1016/j.actaastro.2018.06.021.

[21] R.K. Johnson, F.M. Cheatwood, A.M. Calomino, S.J. Hughes, A.M. Korzun, J.M. DiNonno, M.C. Lindell, G.T. Swanson, HIAD advancements and extension of mission applications, International Planetary Probe Workshop; 13th; 13-17 Jun. 2016; Laurel, MD; United States, 2016.

[22] B. Harper, R.D. Braun, Asymmetrically stacked tori hypersonic inflatable aerodynamic decelerator design study for mars entry, AIAA Atmospheric Flight Mechanics Conference, AIAA, 2014paper 2014-1095.

[23] N. Skolnik, H. Kamezawa, L. Li, G.A. Rossman, B. Sforzo, R.D. Braun, Design of a novel hypersonic inflatable aerodynamic decelerator for mars entry, descent, and landing, AIAA Atmospheric Flight Mechanics Conference, AIAA, 2017paper 2017-0469.

[24] J.S. Green, B. Dunn, R. Lindberg, Morphing hypersonic inflatable aerodynamic decelerator, AIAA Aerodynamic Decelerator Systems (ADS) Conference, AIAA, 2013paper 2013-1256.

[25] P. Wercinski, Adaptable Deployable Entry and Placement Technology (ADEPT), Oral/Visual Presentation ARC-E-DAA-TN31961, NASA.

[26] K. McManus, T. Poinsot, S. Candel, A review of active control of combustion instabilities, Prog. Energy Combust. Sci. 19 (1) (1993) 1–29.

[27] M.L. Webber, Phase Shift Control: Application and Performance Limitations with Respect to Thermoacoustic Instabilities, Ph.D. thesis (2003) Virginia Tech.

[28] J. Hathout, M. Fleifil, A. Annaswamy, A. Ghoniem, J. Hathout, M. Fleifil, A. Annaswamy, A. Ghoniem, Why do secondary peaks occur in experimental active controllers of thermoacoustic instability? 33rd Joint Propulsion Conference and Exhibit, 1997, p. 2834.

[29] W. Saunders, M. Vaudrey, B. Eisenhower, U. Vandsburger, C. Fannin, Perspectives on linear compensator designs for active combustion control, 37th Aerospace Sciences Meeting and Exhibit, 1999, p. 717.

[30] Microsatellite reaction wheels (rw3-0.060), http://www.sinclairinterplanetary.com/reactionwheels, accessed: 2018-05-02.